SILICON MONOXIDE AND METHANOL EMISSION FROM THE NGC 2071 MOLECULAR OUTFLOW

GUIDO GARAY AND DIEGO MARDONES

Departamento de Astronomía, Universidad de Chile, Casilla 36-D, Santiago, Chile

AND

L. F. RODRÍGUEZ

Instituto de Astronomía, UNAM, Apdo. Postal 70-264, 04510 México, D.F., México

ABSTRACT

We report observations of emission in the $J = 3 \rightarrow 2$ and $J = 2 \rightarrow 1$ transitions of SiO and $J_k = 3_k \rightarrow 2_k$ transitions of CH_3OH, made with the Swedish-ESO Submillimeter Telescope (SEST), toward the high-velocity, collimated molecular outflow in NGC 2071. Emission is detected from the lobes, as well as from the central core region, in both species. The spatial distribution of the SiO wing emission, which is detected over a velocity range of ~ 50 km s^{-1}, shows three distinct features: a blueshifted clump located toward the northeast, a redshifted clump located toward the southwest, and a central structure, with moderate redshifted velocities, located near the cluster of young stellar objects. The shape of the SiO profiles from the northeast and southwest clumps are distinctly different. The SiO lines from the northeast clump exhibit a peak near the velocity of the ambient cloud and a gradual decline toward blueshifted velocities reaching flow velocities of up to -32 km s^{-1}. On the other hand, the SiO profiles from the southwest clump show a peak emission at a velocity that is redshifted by ~ 8.5 km s^{-1} from the ambient gas velocity and a gradual decline in brightness toward the ambient cloud velocity. We suggest that the SiO emission from the clumps are signposts of working surfaces where a collimated jet is interacting with ambient material, and ascribe the differences in line shape to differences in the density of the environment under which the jet is propagating.

The abundance of silicon monoxide in the outflow lobes is found to be enhanced, with respect to that of quiescent ambient gas in dark globules, by at least 2 orders of magnitude (peak enhancement ≥ 500 in the southwest clump and ≥ 170 in the northeast clump). The abundance of methanol is considerably more enhanced in the southwest clump (peak enhancement of ~ 500) than in the northwest clump (peak enhancement of ~ 70). We suggest that the large enhancements of methanol and silicon monoxide in the outflow clumps are most likely due to the release from grains of ice mantles and Si-bearing species via shocks produced by the interaction between the outflow and dense ambient gas, and attribute the differences in enhancements to the different shock velocities attained in the northeast clump ($v_s \sim 45$ km s^{-1}) and southwest clump ($v_s \sim 12$ km s^{-1}).

Subject headings: ISM: abundances — ISM: individual (NGC 2071) — ISM: jets and outflows — ISM: molecules

1. INTRODUCTION

The NGC 2071 star-forming region, located $\sim 4'$ north of the reflection nebula NGC 2071, is deeply embedded in the Lynds 1630 dark cloud. It has been identified as an active zone of star formation on the basis that it contains H_2O masers (Schwartz & Buhl 1975; Campbell 1978; Genzel & Downes 1979), OH masers (Pankonin, Winnberg, & Booth 1977), a cluster of infrared sources (Persson et al. 1981; Walther, Geballe, & Robson 1991; Walther et al. 1993), compact radio sources (Bally & Predmore 1983; Snell & Bally 1986; Torrelles et al. 1998), and a bipolar molecular outflow (Lichten 1982; Bally 1982). Far-infrared observations of the region indicate a total luminosity of $\sim 500 \, L_\odot$ (Harvey et al. 1979; Sargent et al. 1981; Butner et al. 1990) for a distance of 390 pc (Anthony-Twarog 1982). The infrared (IR) luminosity and the flux of the radio continuum sources suggest the presence of stars with spectral types in the range B3 to B5, indicating that NGC 2071 is a region of massive star formation.

The molecular flow detected toward NGC 2071 is one of the most energetic bipolar outflows known, exhibiting a full width in the CO($1 \rightarrow 0$) line of 75 km s^{-1} (Bally & Lada 1983). Observations in the $J = 2 \rightarrow 1$ and $J = 1 \rightarrow 0$ lines of CO, made with angular resolutions of $\sim 20''$–$40''$, show a collimated bipolar flow of $\sim 5'$ in length (~ 0.6 pc) with a mean flow velocity, weighted by mass, of ~ 7 km s^{-1} (Snell et al. 1984; Moriarty-Schieven, Snell, & Hughes 1989). In addition, sensitive observations of the emission in the $J = 3 \rightarrow 2$ line of CO, made with $\sim 20''$ resolution, show the presence of an extremely high velocity (EHV; $30 < |v_{LSR} - v_o| < 60$ km s^{-1}, where v_o is the ambient cloud velocity) component of molecular material (Chernin & Masson 1992). In the range of moderate to high flow velocities ($|v_{LSR} - v_o| < 30$ km s^{-1}) the CO emission shows a clumpy, hollow-shell structure (Moriarty-Schieven et al. 1989), which can also be seen in CS and HCO$^+$ (Kitamura et al. 1990; Kitamura, Kawabe, & Ishiguro 1992). The EHV CO flow is more collimated than the high-velocity flow and has compact peaks located approximately halfway along the high-velocity (HV) lobes. Higher angular resolution ($7''$) CO($1 \rightarrow 0$) interferometric observations reveal a compact bipolar molecular jet centered near the radio continuum sources (Scoville et al. 1986). The above results suggest that the outflow toward NGC 2071 consists of two components: a moderate- to high-velocity swept-up flow and a faster jet component (Margulis & Snell 1989). Observations in the

near-infrared (NIR) at 2.12 μm show extensive shock-excited molecular hydrogen emission from the NGC 2071 outflow (Bally & Lane 1982; Simon & Joyce 1983; Lane & Bally 1986; Burton, Geballe, & Brand 1989), that is very well correlated spatially with the HV HCO$^+$ emission (Girart et al. 1999) and has spatial extent and bipolar morphology similar to that of the swept-up CO outflow (Garden, Russell, & Burton 1990).

Collimated outflows are thought to be driven by jets that accelerate the ambient gas through shocks (e.g., Raga & Cabrit 1993), which are expected to produce a significant transformation of the physical and chemical properties of the surroundings. While a considerable progress has been made in the understanding of the physical properties of collimated outflows (see reviews by Bachiller & Gómez-González 1992; Fukui et al. 1993; Bachiller 1996), very little is known about their chemistry. Few multiline mapping of molecular outflows have been performed so far (Blake et al. 1995; Bachiller & Pérez Gutiérrez 1997). The NGC 2071 bipolar flow is an ideal source for a detailed study of the chemical characteristics across collimated shocks. In this paper we report observations of emission in rotational transitions of silicon monoxide (SiO) and methanol (CH$_3$OH), made with the Swedish-ESO Submillimeter Telescope (SEST), toward the NGC 2071 highly collimated outflow. Theoretical calculations predict that these molecules should be good tracers of shocks because their abundance can be changed by several orders of magnitude (Hartquist, Oppenheimer, & Dalgarno 1980; Mitchell 1984; Hollenbach & McKee 1989; Neufeld & Dalgarno 1989; Schilke et al. 1997; Caselli, Hartquist, & Havnes 1997). In fact, recent observations show that both SiO and CH$_3$OH emission are significantly enhanced in outflows (Bachiller, Martín-Pintado, & Fuente 1991; Martín-Pintado, Bachiller, & Fuente 1992; Bachiller et al. 1995; Avery & Chiao 1996; Garay et al. 1998).

2. OBSERVATIONS

The methanol and silicon monoxide observations were carried out using the 15 m SEST located on La Silla, Chile, during 1997 March and 1998 January. The transitions and frequencies observed and the instrumental parameters are summarized in Table 1. We used SiS receivers to simultaneously observe lines at 2 and 3 mm wavelengths. Single-sideband receiver temperatures were typically 120 K for both receivers. As back end we used high-resolution acousto-optical spectrometers providing a channel separation of 41.775 kHz and a total bandwidth of 43 MHz.

Within the available bandwidths, three rotational lines of CH$_3$OH could be observed at 2 mm ($J_k = 3_0 \rightarrow 2_0$ A$^+$, $J_k = 3_{-1} \rightarrow 2_{-1}$ E, and $J_k = 3_0 \rightarrow 2_0$ E lines). The antenna half-power beamwidth, main-beam efficiency of the telescope, and spectral resolution at the observed line frequencies are given, respectively, in columns (4), (5), and (6) of Table 1. The emission in the lines of SiO and CH$_3$OH was mapped within a region of $5' \times 5'$, with $30''$ spacings. The central position is at $\alpha_{1950} = 5^h44^m30^s0$; $\delta_{1950} = 0°20'40''$, which is about $8''$ southwest of IRS1 (Persson et al. 1981). The observations were performed in the position switched mode, with the OFF position located at $\alpha_{1950} = 5^h44^m24^s0$, $\delta_{1950} = 0°17'40''$. The integration times on source per position and the resulting rms noise in antenna temperature are given, respectively, in columns (7) and (8) of Table 1.

In addition, during 1999 January we made SEST observations of the CO and ^{13}CO emission in the $J = 1 \rightarrow 0$ and $2 \rightarrow 1$ lines toward three selected positions, at offsets from the central position of ($60''$, $60''$; blue SiO peak), ($-90''$, $-90''$; red SiO peak) and ($0''$, $0''$). The observations were performed in the position switched mode, with the OFF position located at $\alpha_{1950} = 05^h41^m30^s0$, $\delta_{1950} = -0°10'0''$. The goal of these observations was to obtain sensitive data in order to determine CO column densities over a wide range of flow velocities, which in turn will permit to derive abundance enhancements relative to CO.

3. RESULTS

3.1. Line Profiles

Figure 1 shows the spectra observed toward the NGC 2071 star-forming region in the three transitions mapped with SEST with $30''$ spacings. SiO emission is detected at blueshifted velocities, with respect to the systemic ambient cloud velocity of 9.6 km s^{-1} (Wootten et al. 1984; Girart et al. 1999), toward the northeast region of the map, at moderate redshifted velocities toward the central region, and at higher redshifted velocities toward the southwest region. On the other hand, the CH$_3$OH profiles from the northeast region show strong emission from gas at the velocity of the ambient cloud and very weak emission from gas at blueshifted velocities; toward the central region they show a mixture of strong emission from gas at the velocity of the ambient cloud and from a broad redshifted feature with a peak velocity relative to the quiescent cloud velocity of ~ 6.5 km s^{-1}; finally toward the southwest the profiles exhibit mainly emission from high-velocity redshifted gas with no, or very weak, emission from gas at the velocity of

TABLE 1

OBSERVATIONAL PARAMETERS

Molecule (1)	Transition (2)	Frequency (MHz) (3)	Beam Size (FWHM ") (4)	η (5)	Δv^a (km s^{-1}) (6)	Integration Time (min.) (7)	Noise[b] (K) (8)
CH$_3$OH......	$J_k = 3_{-1} \rightarrow 2_{-1}$ E	145097.470	34	0.66	0.086	4	0.070
SiO	$J = 2 \rightarrow 1$	86846.998	57	0.75	0.144	6	0.031
	$J = 3 \rightarrow 2$	130268.702	40	0.68	0.096	4	0.045
CO	$J = 1 \rightarrow 0$	115271.204	45	0.70	0.109	4	0.16
	$J = 2 \rightarrow 1$	230537.990	23	0.60	0.054	4	0.11
^{13}CO	$J = 1 \rightarrow 0$	110201.352	45	0.70	0.114	30	0.028
	$J = 2 \rightarrow 1$	220398.686	23	0.60	0.057	30	0.023

[a] Channel separation.
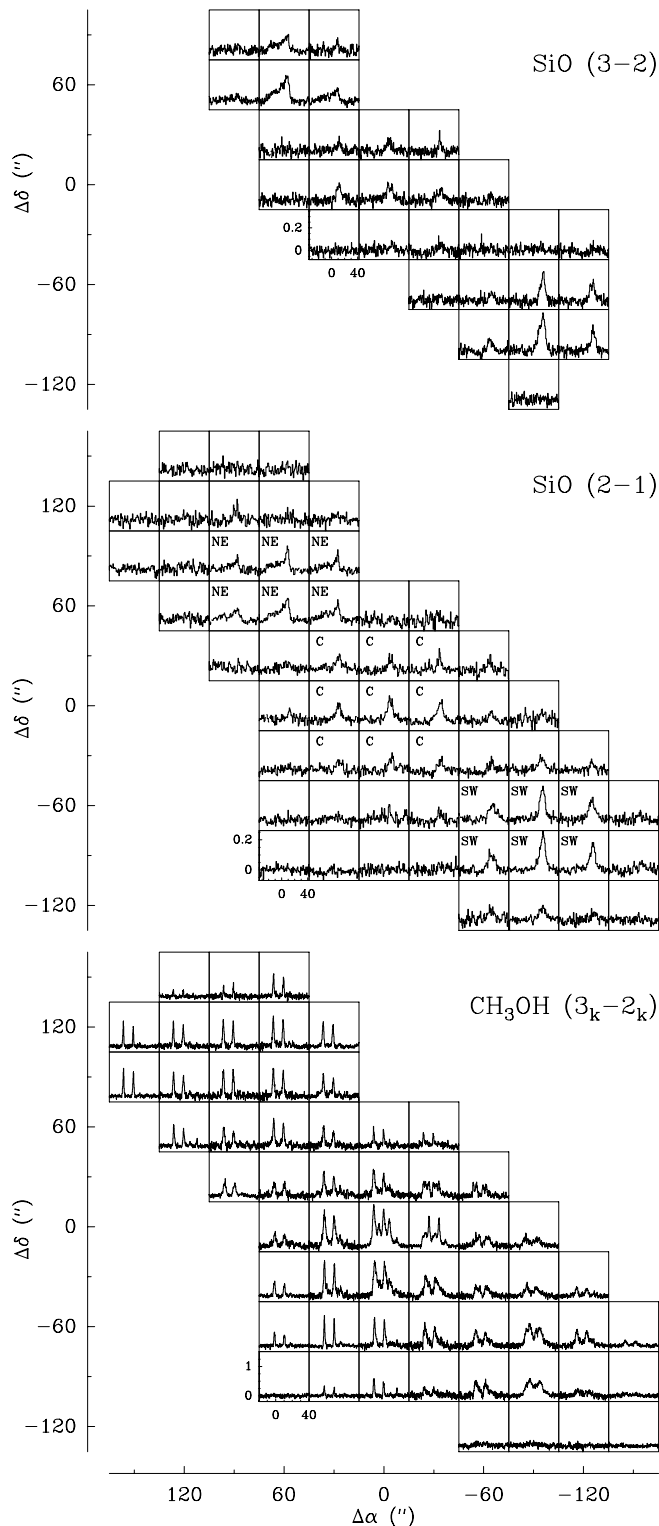[b] 1σ rms noise in antenna temperature.

FIG. 1. —Observed spectra of the silicon monoxide and methanol line emission within the $5' \times 5'$ central region of the NGC 2071 massive star-forming region. The grid spacing is $30''$. Offsets are from the reference position at $\alpha_{1950} = 5^h44^m30^s.0$, $\delta_{1950} = 0°20'40''$. The velocity scale ranges from -35 to 42 km s^{-1} in the spectra of silicon monoxide and from -20 to 40 km s^{-1} in the spectra of methanol. The antenna temperature scale is from -0.07 to 0.26 K for SiO($2 \to 1$), from -0.08 to 0.36 K for SiO($3 \to 2$), and from -0.2 to 1.5 K for CH₃OH($3_k - 2_k$).

the quiescent gas. The methanol wing emission is considerably stronger toward the southwest region than toward the northeast region.

The differences in line profiles with flow position are illustrated in more detail in Figure 2, which shows the spectra of the SiO and CH₃OH line emission averaged across positions (indicated in the middle panel of Fig. 1) in the northeast, central, and southwest regions. The average line profile of the SiO emission from the southwest exhibits a strong peak at v_{LSR} of ~ 18 km s^{-1}, redshifted from the ambient cloud velocity by about 8.5 km s^{-1}, a rapid decrease in intensity toward redder velocities, and a slower decline toward the ambient cloud velocity. On the other hand, the average profile of the SiO emission from the northeast shows a peak at the velocity of the ambient cloud, a gradual decrease in intensity toward large blueshifted velocities (up to v_{LSR} of -22.5 km s^{-1}), and a steep decline toward redder velocities. The methanol spectrum from the central region shows emission from at least two components: one at the velocity of the ambient cloud and the other at a velocity redshifted by ~ 6.5 km s^{-1} with respect to the quiescent gas. The methanol spectrum from the southwest clump shows only emission from redshifted gas, with LSR velocities ranging from ~ 10 km s^{-1} to ~ 22 km s^{-1}.

3.2. Morphology and Kinematics

The velocity structure of the emission in the CH₃OH($3_k \to 2_k$) lines and SiO($1 \to 0$) transition is presented in Figure 3, which shows position-velocity (p-v) maps along a direction with a P.A. of $45°$ passing through the (0,0) position. The methanol diagram displays simultaneously the p-v characteristics of the emission in all three observed transitions, and hence the features seen in this diagram do not solely reflect the kinematics of the gas but also overlap of the emission between these three components. In spite of this, this diagram clearly shows that the methanol lines from the central region cover a broad range of velocities, spanning from the ambient cloud velocity up to flow velocities of ~ 8.6 km s^{-1}. The flow velocity is defined as $v_{flow} = v_{LSR} - v_o$, where v_o is the velocity of the emission from quiescent ambient gas. The methanol p-v feature from the central region can be roughly characterized as being produced by three components: (1) a strong feature at the velocity of the quiescent ambient gas; (2) a low-velocity redshifted component, with a peak flow velocity of 2.9 km s^{-1}; and (3) a moderate-velocity redshifted component, with a peak flow velocity of 6.5 km s^{-1}. The methanol emission from the southwest, whose peak is located at $\sim 127''$ southwest of the central energy sources, arises solely from redshifted gas. The integrated methanol emission can be characterized as arising from a low-velocity component, with a peak flow velocity of 2.9 km s^{-1} and a width of 4.2 km s^{-1}, and a moderate to intermediate velocity component, with a peak flow velocity of 7.8 km s^{-1} and a width of 6.2 km s^{-1}. Toward the northeast the methanol lines show strong emission from gas at the velocity of the ambient cloud and very weak emission at blueshifted velocities from a feature whose peak position is located $\sim 84''$ from the central sources.

The silicon monoxide p-v diagram shows that the emission from the southwest region has a similar velocity structure to that of the methanol emission, exhibiting a peak at v_{LSR} of 18.1 km s^{-1} and covering a range in velocity that extends from the ambient cloud velocity up to a v_{LSR} of ~ 26
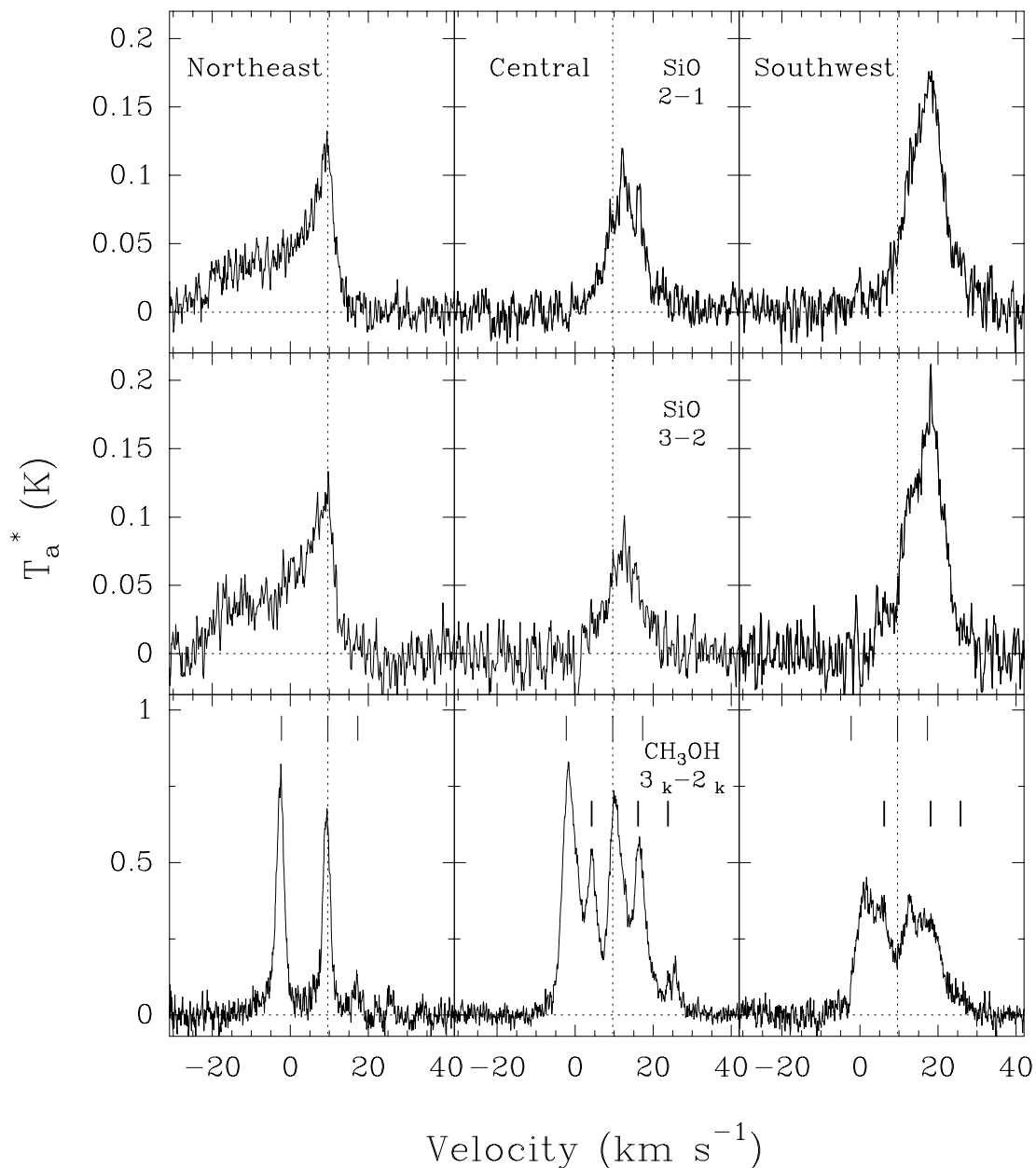
Fig. 2.—Spectra of the spatially integrated line emission from the northeast clump, central region, and southwest clump of the NGC 2071 region. Transitions are given in the upper right-hand corner of the spectra shown in the middle column. The vertical dotted line indicates the systemic velocity of the ambient gas of 9.6 km s^{-1}. The vertical bars shown at the top of the methanol spectra mark the expected positions of the three rotational transitions, within the observed velocity range, for ambient gas. In the central and southwest spectra we also mark (*short vertical bars near the center*) the expected positions of the rotational transitions for a gas moving at velocities relative to the ambient gas of 6.5 and 8.5 km s^{-1}, respectively.

km s^{-1} ($v_{\text{flow}} \sim 16$ km s^{-1}). On the other hand, the SiO emission from the northeast is remarkably different from that of methanol, exhibiting a striking high-velocity blue-shifted feature that extends up to a v_{LSR} of -22.5 km s^{-1} ($v_{\text{flow}} \sim -32.1$ km s^{-1}). No corresponding feature is detected in the lines of CH$_3$OH. Toward the central region the SiO emission arises from the two redshifted components seen in methanol, with no, or very weak, emission being detected at the velocity of the ambient cloud.

The spatial distribution of the SiO emission at different flow velocities are presented in Figure 4, which shows maps of the velocity integrated wing SiO emission in four flow velocity ranges (low: 2–5 km s^{-1}; moderate: 5–9 km s^{-1}; intermediate: 9–15 km s^{-1}; and high: 15–32 km s^{-1}). At

low and moderate flow velocities the spatial distribution is characterized by exhibiting a blueshifted structure toward the northeast and two redshifted structures: one centered around and the other located southwest of the central energy sources. At intermediate flow velocities the spatial distribution of the SiO emission clearly breaks up into separated blueshifted and redshifted clumps. The blue-shifted SiO clump resides roughly halfway along the CO blueshifted lobe, has a peak position located at $\sim 77''$ northeast from the central energy sources and a deconvolved angular size (FWHM) of $47''$. The redshifted SiO clump has a deconvolved size of $47''$, its peak is offset from the radio sources by $\sim 130''$ toward the southwest, and it is located nearly at the outer edge of the redshifted CO lobe. At high
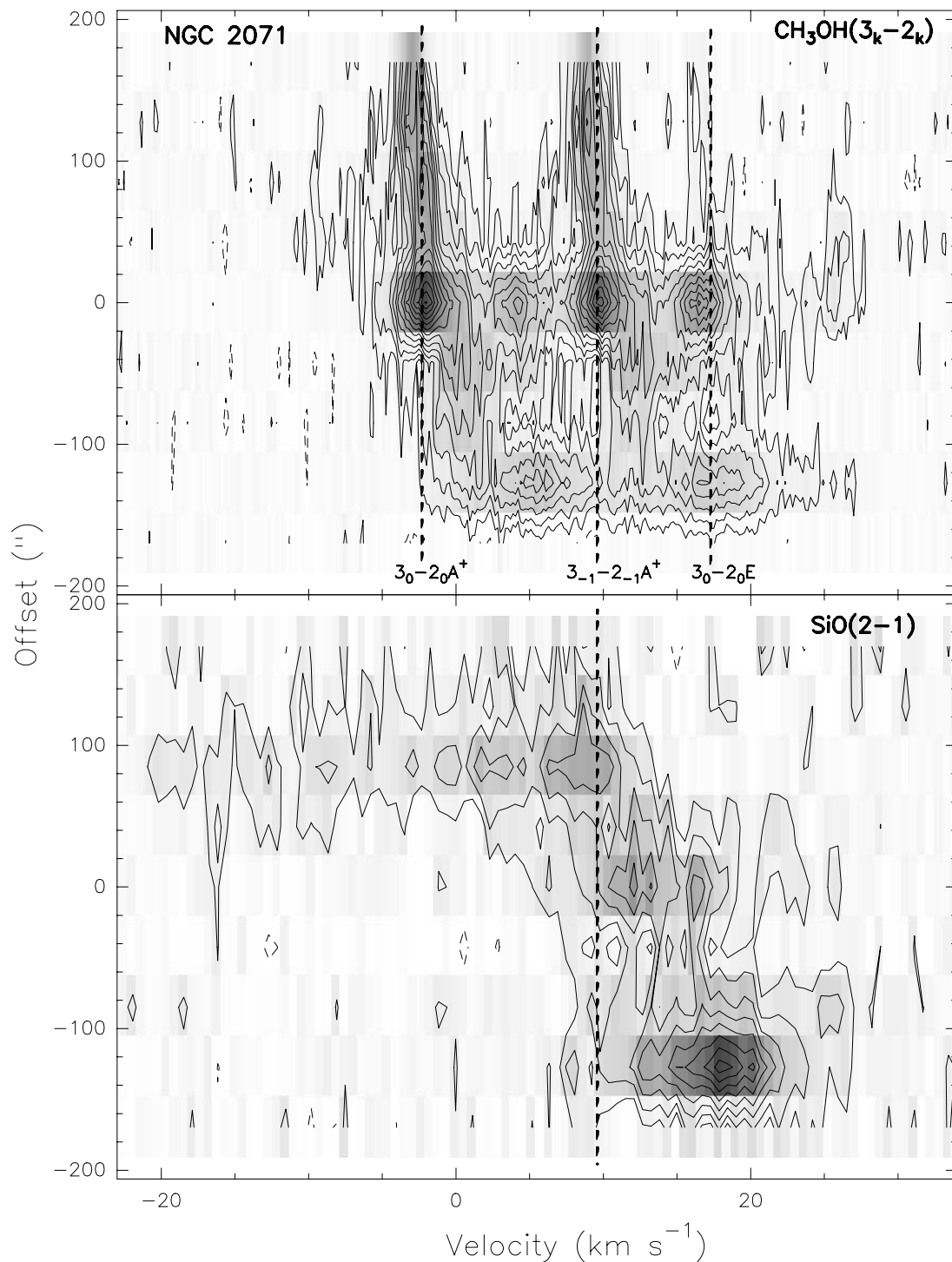
Fig. 3.—Position-velocity diagram of the molecular emission along the symmetry axis of the outflow. *Top:* CH$_3$OH($3_k \to 2_k$). Contour levels are drawn at -0.1 K, and from 0.1 K to 1.4 K in steps of 0.1 K. The vertical dotted lines indicate the positions of the different k-components for a systemic velocity of 9.6 km s^{-1}. *Bottom:* SiO($2 \to 1$). Contour levels are drawn at -0.03 K, and from 0.03 to 0.24 K in steps of 0.03 K. The vertical dotted line indicates the systemic velocity of the ambient gas of 9.6 km s^{-1}.

flow velocities the SiO emission only arises from the northeast blueshifted clump. The blue and red SiO clumps are roughly aligned in a direction with a position angle of $\sim 44°$.

The determination of the spatial distribution of the methanol emission in the velocity ranges discussed above is hindered by the considerable blending of the emission between the different k-components. Using the emission in the

$3_0 \to 2_0$ A^+ component it is possible, however, to determine the spatial distribution of methanol in the low and moderate ranges of flow velocities. The bottom panels in Figure 4 present maps of the methanol emission integrated over these velocity ranges. The morphology of the redshifted wing emission in these velocity ranges is similar in both molecular species, although there are differences in the relative intensities. The intensity of the methanol emission from
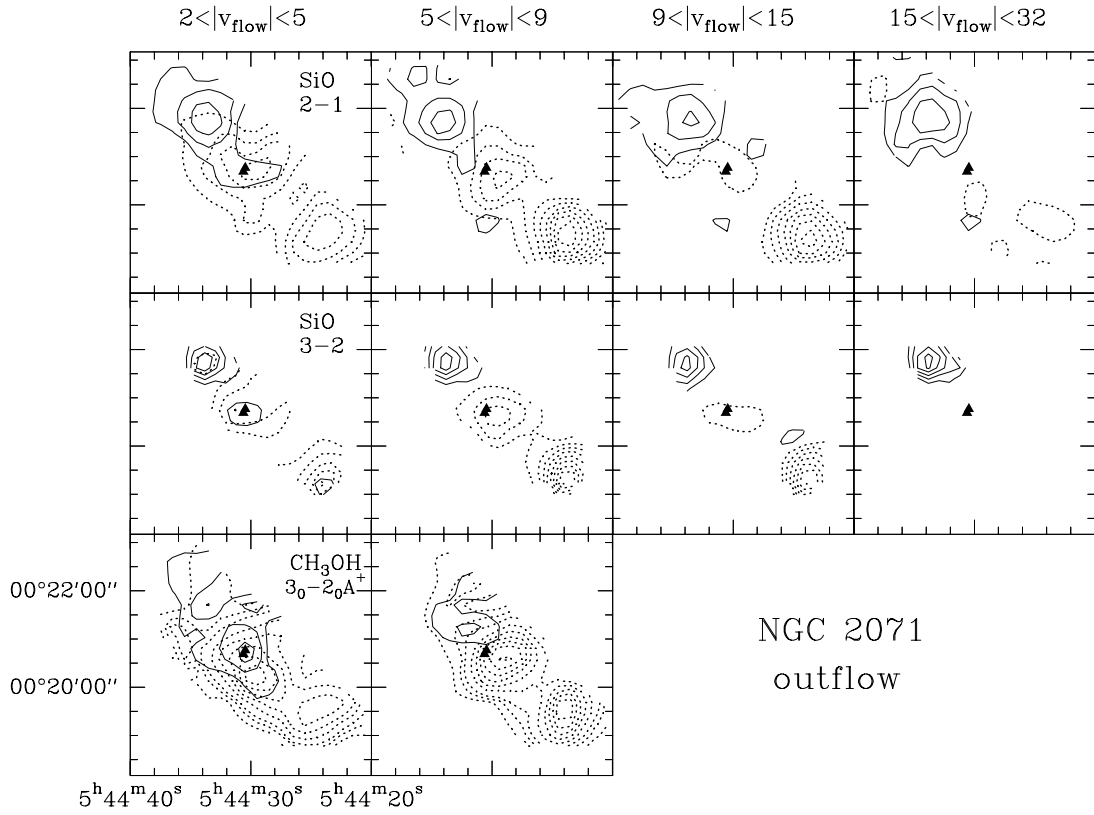
FIG. 4.—Contour maps of velocity-integrated line wing emission from the NGC 2071 bipolar outflow. Continuous lines represent blueshifted emission, dashed lines redshifted emission, and the triangles mark the position of the radio continuum sources IRS1 and IRS3 (Torrelles et al. 1998). *Left*: Low-velocity range. *Middle left*: Moderate-velocity range. *Middle right*: Intermediate-velocity range. *Right*: High-velocity range. The lowest contour and contour interval are, from left to right, 0.09, 0.10, 0.11, and 0.19 K km s^{-1} for SiO($2 \to 1$), 0.12, 0.12, 0.15, and 0.20 K km s^{-1} for SiO($3 \to 2$), and 0.15 K km s^{-1} in both panels for CH$_3$OH($3_0 - 2_0 A^+$).

TABLE 2

DERIVED SILICON MONOXIDE PARAMETERS

v_{flow} (km s^{-1})	SiO T_R (K)	N_v (10^{11} cm^{-2})	CO N_v (10^{16} cm^{-2})	[SiO/CO]	ENHANCEMENT
		Red lobe ($-90''$, $-90''$)			
$1.4 \to 3.4$.............	45 ± 9	12 ± 2	19 ± 3	6.2×10^{-6}	210
$3.4 \to 5.4$.............	16 ± 3	11 ± 3	14 ± 3	7.7×10^{-6}	260
$5.4 \to 7.4$.............	14 ± 3	11 ± 3	8.7 ± 1.7	1.3×10^{-5}	430
$7.4 \to 9.4$.............	14 ± 3	12 ± 2	8.1 ± 1.6	1.5×10^{-5}	500
$9.4 \to 11.4$	13 ± 3	11 ± 3	8.3 ± 1.7	1.3×10^{-5}	430
$11.4 \to 13.4$	20 ± 4	7 ± 2	7.9 ± 1.6	9.1×10^{-6}	300
		Blue lobe ($60''$, $60''$)			
$-18.6 \to -16.6$......	29 ± 6	4.9 ± 0.8	14 ± 3	3.5×10^{-6}	120
$-16.6 \to -14.6$......	22 ± 4	4.9 ± 0.9	15 ± 3	3.3×10^{-6}	110
$-14.6 \to -12.6$......	50 ± 10	5.3 ± 1.0	13 ± 3	4.1×10^{-6}	140
$-8.6 \to -6.6$	18 ± 4	6.7 ± 0.9	13 ± 3	5.2×10^{-6}	170
$-6.6 \to -4.6$	21 ± 4	6.7 ± 0.9	21 ± 4	3.2×10^{-6}	110
$-2.6 \to -0.6$	20 ± 4	9.0 ± 1.1	340 ± 17	2.6×10^{-7}	9
$-0.6 \to 1.4$	17 ± 3	8.0 ± 0.9	280 ± 14	2.9×10^{-7}	10
$1.4 \to 3.4$..............	25 ± 5	5.2 ± 0.8	31 ± 5	1.7×10^{-6}	57
$3.4 \to 5.4$..............	15 ± 3	3.3 ± 0.6	17 ± 3	1.9×10^{-6}	63
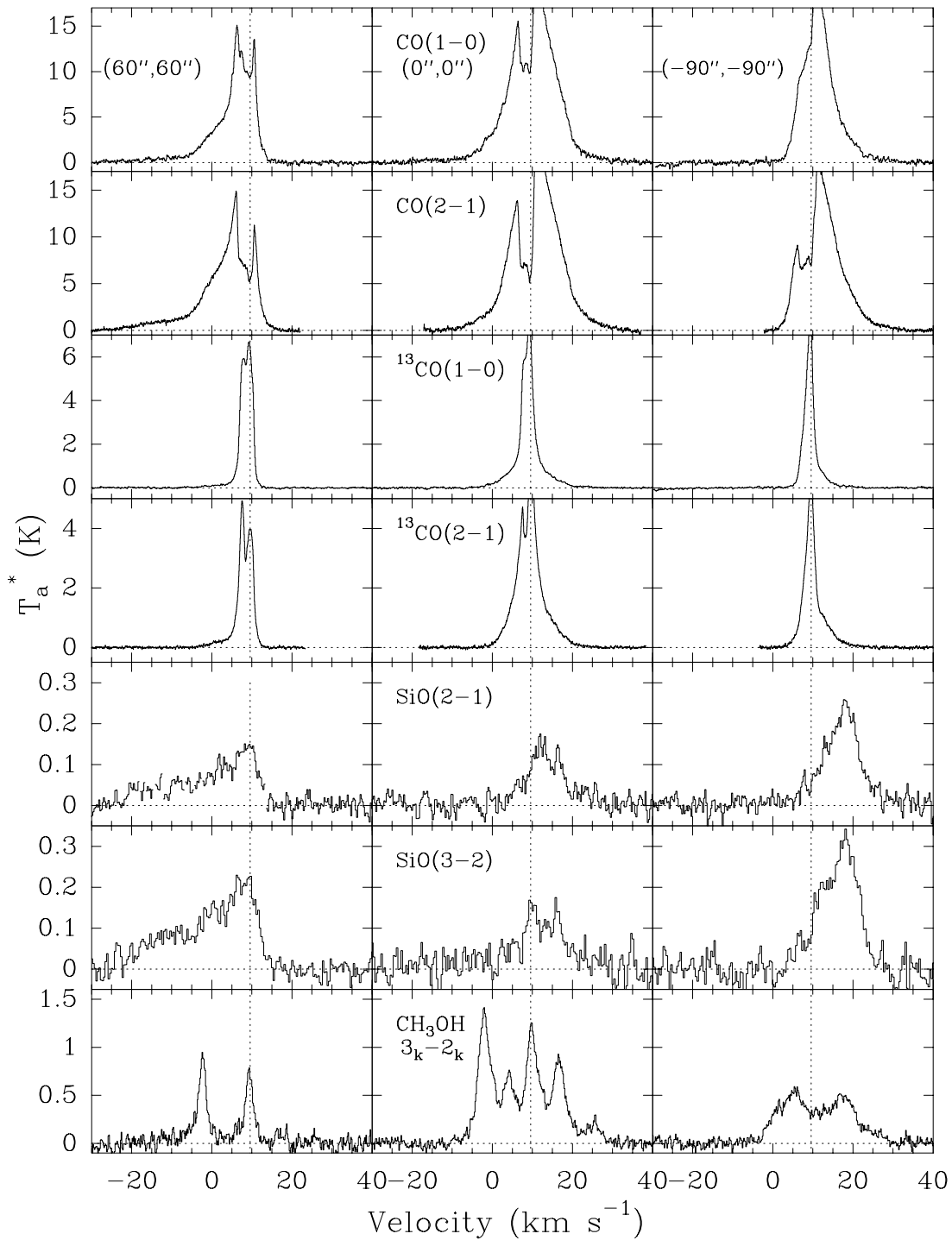
FIG. 5.—Line profiles of the $^{12}CO(J = 1 \to 0)$, $^{12}CO(J = 2 \to 1)$, $^{13}CO(J = 1 \to 0)$, $^{13}CO(J = 2 \to 1)$, $SiO(J = 2 \to 1)$, $SiO(J = 3 \to 2)$, and $CH_3OH(J_k = 3_k \to 2_k)$ emission observed toward selected positions of the NGC 2071 outflow. The vertical dotted lines indicate the systemic velocity of the ambient gas of 9.6 km s⁻¹.

the central region is stronger than toward the southwest clump, whereas in SiO the emission from the clump is stronger. On the other hand, the blueshifted methanol emission from the northwest lobe is considerably weaker than that in silicon monoxide.

3.3. Column Densities and Rotational Temperatures

Column densities and temperatures, as well as abundances (see § 4.3), were computed toward three selected

positions of the outflow: peak of northeast clump (60″,60″), peak of southwest clump (−90″,−90″), and central position (0″,0″). The observed spectral line profiles used in these computations are shown in Figure 5. For silicon monoxide and methanol the column density in the velocity range $(v, v + \Delta v)$, N_v, and rotational temperature, T_{rot}, were derived from a rotational diagram analysis (see, e.g., Linke, Frerking, & Thaddeus 1978; Blake et. al 1987), with the assumptions of optically thin conditions and local thermo-

TABLE 3

DERIVED METHANOL PARAMETERS

| v_{flow} (km s^{-1}) | CH$_3$OH | | CO | | |
	T_R (K)	N_v (10^{14} cm^{-2})	N_v (10^{16} cm^{-2})	[CH$_3$OH/CO]	ENHANCEMENT
Red lobe ($-90''$, $-90''$)					
$5.5 \rightarrow 6.5$	10.6 ± 1.6	3.1 ± 0.3	3.2	9.5×10^{-3}	320
$6.5 \rightarrow 7.5$	8.7 ± 1.7	3.9 ± 0.6	3.2	1.2×10^{-2}	400
$7.5 \rightarrow 8.5$	7.0 ± 1.1	5.2 ± 0.8	3.5	1.5×10^{-2}	500
$8.5 \rightarrow 9.5$	7.0 ± 1.4	5.1 ± 1.0	4.5	1.1×10^{-2}	370
$9.5 \rightarrow 10.5$	7.6 ± 1.6	4.5 ± 0.9	4.6	9.8×10^{-3}	330
$10.5 \rightarrow 11.5$	6.2 ± 1.0	4.4 ± 0.8	4.1	1.1×10^{-2}	370
Blue lobe ($60''$, $60''$)					
$-4.0 \rightarrow -3.0$	5.9 ± 1.2	3.6 ± 0.9	17.	2.1×10^{-3}	70
$-3.0 \rightarrow -2.0$	5.2 ± 0.9	3.7 ± 0.9	90.	4.1×10^{-4}	14
$-2.0 \rightarrow -1.0$	7.6 ± 1.3	5.5 ± 0.9	190.	2.9×10^{-4}	10
$-1.0 \rightarrow 0.0$	6.1 ± 1.1	7.2 ± 1.5	250.	2.9×10^{-4}	10

dynamical equilibrium (LTE), which relates the integrated line intensity, rotational temperature, and column density via

$$\frac{3k \int_v^{v+\Delta v} T_{mb}\, dv}{8\pi^3 \mu^2 \nu S} = \frac{N_v}{Q(T_{\text{rot}})} \exp\left(-\frac{E_u}{kT_{\text{rot}}}\right), \qquad (1)$$

where μ, ν, and S are the transition dipole moment, frequency, and line strength of the transition, respectively, $\int_v^{v+\Delta v} T_{mb}\, dv$ is the velocity-integrated main-beam brightness, obtained directly from the observations, E_u is the upper state energy, and $Q(T_{\text{rot}})$ is the rotational partition function. The column densities of CO molecules were computed from the ratio of the observed emission in the ^{12}CO and ^{13}CO lines assuming an isotopic [^{12}CO/^{13}CO] abundance ratio of 73 (Choi, Evans, & Jaffe 1993) and an excitation temperature for the HV gas of 25 K (Chernin & Masson 1992; see Bourke et al. 1997 for a description of the method). We note that owing to the low strength of the ^{13}CO emission in the outer wings this method allowed us to compute column densities for flow velocities up to $\sim \pm 18$ km s^{-1}. Table 2 gives the column densities and rotational temperatures of SiO in different ranges of flow velocity, derived by integration of the emission in velocity intervals of 2 km s^{-1}. Table 3 gives the column densities and rotational temperatures of CH$_3$OH in different ranges of flow velocity, derived by integration of the emission in velocity intervals of 1 km s^{-1}.

4. DISCUSSION

The observed characteristics of the line wing emission provide useful diagnostics of the nature of the mechanism that gives rise to the high-velocity molecular gas. Its spatial distribution help to discern whether the high-velocity flows are produced by jets or by collimated wide angle winds, while its spectral signatures help to identify the type of shock that produces the wing emission. In J-type shocks the cooling gas is fully accelerated and thus emits a line displaced from the velocity of the quiescent cloud by about the shock velocity, v_s. The line is relatively narrow since all the emission occurs between velocities of $\frac{3}{4}v_s$ and v_s. In C-type shocks most of the emission occurs when the gas is just

being accelerated; thus an observer at rest with respect to the preshock gas would see a smooth, broad emission profile with a peak near the velocity of the quiescent cloud (see Hollenbach 1997). The distinction between the type of shock associated with a molecular outflow from its spectral characteristics is not straightforward, however, particularly since molecular outflows are believed to be associated with bow shocks which may have J-shock characteristics at the apex and C-shock characteristics in the wake (Smith & Brand 1990).

The profiles of the SiO line emission from the northeast and southwest clumps of NGC 2071 show distinct differences in their shapes, other than, of course, in the expected velocity reversal. In addition, the spatial distribution of the SiO emission from the lobes is not symmetric with respect to the central energy sources and is different to that traced by the CO emission. These differences suggest that the jet and/or wind interaction with the ambient material is probably different in the southwest than in the northeast. Different type of shocks might develop as a result of differences in the physical conditions of the ambient gas and/or in the fractional ionization. Below we discuss possible explanations for the origin of the SiO and CH$_3$OH emission from the lobes of the NGC 2071 outflow.

4.1. The Southwest SiO Clump

The southwest SiO clump is found projected near the outer edge of the redshifted lobe traced in the $J = 1 \rightarrow 0$ and $J = 2 \rightarrow 1$ lines of CO (Snell et al. 1984; Moriarty-Schieven et al. 1989). The SiO line profiles show a peak at a velocity that is redshifted by roughly 8.5 km s^{-1} from the ambient cloud velocity, a gradual decline in brightness from the peak velocity ($v_{\text{LSR}} \sim 18.1$ km s^{-1}) toward the ambient cloud velocity and a more rapid decline toward higher velocities. The spatial location, close to the outer edge of the corresponding CO outflow, and the shift of the velocity peak away from the velocity of the preshock gas hint that the southwest SiO clump might mark a region where a supersonic jet or highly collimated wind is currently processing ambient gas through a shock.

Adopting a simple model in which the jet drives a slab of shocked material, bounded on one side by a jet shock where

the jet material is decelerated and on the other by an ambient shock in which the ambient material is accelerated (see Hollenbach 1997), then in steady state the slab velocity, v_s, is given by

$$v_s = \frac{v_j}{[1 + \sqrt{(\rho_a/\rho_j)}]}, \qquad (2)$$

where v_j is the jet velocity, ρ_j the jet density, and ρ_a the ambient medium density. Masson & Chernin (1993) find that this type of model is appropriate for a jet propagating in a dense ambient medium, in which case the strong cooling of the shocked material results in a momentum conserving snowplow of ambient gas. From the observed radial flow velocity of 8.5 km s^{-1}, assuming an inclination of the outflow axis with respect to the plane of the sky of 45° (Moriarty-Schieven et al. 1989), we estimate that $v_s = 12$ km s^{-1}. To accelerate the ambient medium to this velocity, assuming $v_j = 200$ km s^{-1} the typical value of jets (Mundt 1986), the simple dynamical model requires the presence of a light (i.e. $\rho_j \ll \rho_a$) jet with $\rho_j/\rho_a = 4 \times 10^{-3}$. There are no determinations of the density of the neutral jet nor of the ambient cloud density at the location of the southwest lobe. It appears, however, that a dense clump is located near the end of the redshifted lobe (Kitamura et al. 1990). Adopting $\rho_a = 1 \times 10^5$ cm^{-3} (Kitamura et al. 1990), we derive that the jet density is $\rho_j \sim 4 \times 10^2$ cm^{-3}. Further, assuming a typical value for the jet radius of 2×10^{16} cm (Mundt, Brugel, & Bührke 1987), the implied jet mass-loss rate is 3×10^{-7} $M_\odot$ yr^{-1}. In a timescale of 10^5 yr the jet will inject 0.03 $M_\odot$ that will entrain and accelerate ~ 0.6 $M_\odot$ of ambient gas. This value is in good agreement with the mass of 0.8 $M_\odot$ determined by Moriarty-Schieven et al. (1989).

While this simple model provides a straightforward explanation of the observed bulk flow velocity, it does not predict the observed asymmetries in the line profiles. The shallow decline in the intensity of the wing emission from the peak toward lower velocities hints the presence of a broad range of shock velocities. The observed wide and asymmetric line profiles are typical of bow shocks, which in fact are expected to form in the interaction of the jet with the ambient medium. Models of the flow of ambient gas induced by the passage of a working surface have been investigated by Raga & Cabrit (1993), Masson & Chernin (1993), and Chernin et al. (1994). In the jet driven model of Masson & Chernin (1993) it is assumed that the thermal pressure of the hot shocked gas drives the shocked material away from the jet axis creating a cocoon which accelerates a shroud of swept-up material. The pressure in the cocoon is rapidly dissipated and the cooled shocked material sweeps up a dense shell in a momentum conserving snowplow phase. Behind the jet head the shroud moves outward in a snowplow fashion and slows down as it sweeps up ambient gas.

We propose that the southwest SiO clump marks the place where a collimated fast jet is transferring momentum to the ambient gas through a nondissociative bow shock. The interaction of the jet with a dense medium gives rise to a strongly dissipative jet head producing a working surface moving at much lower velocities than the jet. This hypothesis is supported by the close spatial association between the southwest SiO clump and the H$_2$ emission from the southwest region (Garden et al. 1990) together with the characteristics of the H$_2$ emission. Burton et al. (1989) found

that at the peak position of the southwest molecular hydrogen feature the H$_2$ lines have narrow line profiles (FWHM < 30 km s^{-1}) and line center velocities close to the ambient cloud velocity (~ 10 km s^{-1}), suggesting that the H$_2$ emission is probably associated with low-velocity shocks in the swept-up gas. We suggest that the bulk of the SiO emission arises from swept-up material at the wake of the bow shock, with a typical radial flow velocity of 8.5 km s^{-1}. The velocity of the gas at the head of the bow shock (see eq. [1]) is not known. A lower limit of 16 km s^{-1} is provided by the terminal radial flow velocity derived from the spectra of the SiO emission.

4.2. *The Northeast* SiO *Clump*

The line profiles of the SiO emission from the northeast clump are notable for exhibiting a broad (~ 30 km s^{-1}), highly asymmetric, blueshifted feature. The shape of the line profiles, showing a strong peak at the velocity of the ambient cloud, a steep decline toward redshifted velocities, and a gradual decrease in intensity from the peak toward blueshifted velocities, suggests that a small fraction of the molecular gas is being accelerated to high velocities while the majority is still moving close to the preshock velocity. The presence of blueshifted gas extending to much higher velocities than the redshifted gas is also evident in the maps of high-velocity OH (Ruiz et al. 1992). The northeast SiO clump is spatially coincident with a broad blueshifted velocity feature detected in SO by Chernin & Masson (1993), both of which exhibit terminal flow velocities of ~ -32 km s^{-1}. Furthermore, its peak position is located roughly at the outer edge of the extreme high-velocity ($|v_{LSR} - v_o| > 30$ km s^{-1}) emission feature reported by Chernin & Masson (1992) in the $J = 3 \rightarrow 2$ line of CO, which has a terminal velocity about twice that of the SiO feature. These large terminal velocities suggest that the northeast SiO clump also marks the location where ambient gas is being processed by jets. A further remarkable characteristic of the northeast SiO clump is the absence of high-velocity wing emission in the CH$_3$OH lines.

We suggest that the northeast SiO clump marks the location where a fast jet is transferring momentum to the ambient medium through prompt entrainment. We envision that in this location the swept up material is being accelerated by a faster bow shock than that toward the southwest clump, producing a bow shock that cools less rapidly than that toward the southwest. This hypothesis is supported by the position-velocity diagram of the SiO emission from this clump (see lower panel of Fig. 3), which bears a notable resemblance to the sharp bend (or hook) at high velocities predicted by Chernin & Masson's model at the position of the bow shock. Fast bow shocks are likely to produce a dissociative shock near the jet head and a continuum of nondissociating C-type shocks of smaller velocities at the wake of the bow. The later shocks accelerate molecules gradually and can preserve molecules in shocks of up to 50 km s^{-1} (Draine, Roberge, & Dalgarno 1983). The observed line profiles suggest then that the SiO emission arises from C-shocks which are restricted to the bow wake. The particular location of the northeast SiO clump, half way along the swept-up low velocity CO flow, can be explained if the direction of the jet wanders, accelerating material in the shell of the low-velocity outflow. This situation is apparently found in several outflows (e.g., Garden et al. 1990; Reipurth 1991).

The H$_2$ emission from the northeast region of NGC 2071 extends over most of the blueshifted low-velocity CO lobe and can be roughly divided into three regions: (1) an inner region close to the cluster of young stellar objects; (2) a middle region featuring a narrow stringlike structure composed of several clumps interconnected by weaker line emission; and (3) an outer region close to the outer edge of the blueshifted CO lobe (Girart et al. 1999). The northeast SiO clump is spatially associated with the H$_2$ stringlike emission from the middle region. The peak velocity of the H$_2$ emission at a position in this region (offset of [20″,50″] with respect to IRS1) is blueshifted by ~ 27 km s^{-1} with respect to the ambient cloud velocity (Burton et al. 1989). Most likely the bulk of the H$_2$ emission arises from gas near the head of the bow, where the velocities are higher, while the bulk of the SiO emission arises from material principally at the wake where the flow velocities are smaller than at the head, possibly producing a series of nondissociative shocks (e.g., Richer, Hills, & Padman 1992).

Why does the jet interaction with the ambient medium produce different line profiles toward the northeast and southwest? A simple explanation is that the observed differences are due to differences in the physical conditions of the environmental material across the NGC 2071 cloud. Density gradients and/or density inhomogeneities should have an important effect since they cause variations in the shock velocity with distance to the source. We suggest that the preshock densities at the position of the northeast clump are lower than that at the position of the southwest clump. In the southwest the interaction of the jet with a dense medium gives rise to a low-velocity nondissociative bow shock. On the other hand, toward the northeast the interaction of the jet with the low-density medium produces a fast bow shock with a dissociative shock at the head. Assuming $v_s = 45$ km s^{-1} (equal to the terminal radial velocities in SiO and SO, of 32 km s^{-1}, corrected by the inclination angle) and using $\rho_j \sim 4 \times 10^2$ cm^{-3} (see § 4.1), we find that the preshock gas density in the northeast clump is 5×10^3 cm^{-3}. This value is probably representative of the density in the filled cavity created after the passage of a previous jet. In addition, the bright SiO emission observed toward the northeast clump at the velocity of the ambient cloud may also find an explanation on the presence of a dissociative shock. The UV radiation generated by the fast shock produces the release of atoms and ions from the mantle of dust particles in the ambient medium, triggering an active photochemistry. Thus the low-velocity SiO emission may arise from hot ambient, nonshocked, gas heated by the copious ultraviolet radiation emitted by the front dissociative shock region at the head of a fast bow shock. On the other hand, since the velocities at the head of the bow shock are probably larger than the shock velocity required to dissociate the molecular hydrogen, of ~ 30 km s^{-1} (Kwan 1977), some of the high-velocity SiO emission may arise from reformed molecules behind the dissociating shock (Neufeld & Dalgarno 1989; Hollenbach & McKee 1989).

4.3. Chemical Enhancement

The chemical composition of a gas cloud is usually characterized by the fractional abundance of molecules relative to molecular hydrogen, the main constituent of the interstellar gas. The abundance of H$_2$ in the lobes of the NGC 2071 outflow is however difficult to estimate. Therefore, in

the following discussion we will consider abundances relative to the CO abundance which can be directly derived from our observations. The fractional abundance of species X, [X/CO] (where X = SiO or CH$_3$OH), is computed as the ratio of the column density of species X, obtained from the rotational analysis (see Tables 2 and 3), and the CO column density in the corresponding velocity range, obtained from the observations of the CO and ^{13}CO lines. The dependence of [SiO/CO] fractional abundance with absolute value of flow velocity observed at the outflow lobes (*open circles:* peak of northeast clump; *filled circles:* peak of southwest clump) and at the central position are shown in the upper and middle panels of Figure 6, respectively. The [CH$_3$OH/CO] abundance ratio versus flow velocity, observed at the peak position of the northeast and southwest SiO clumps, is plotted in the lower panel of
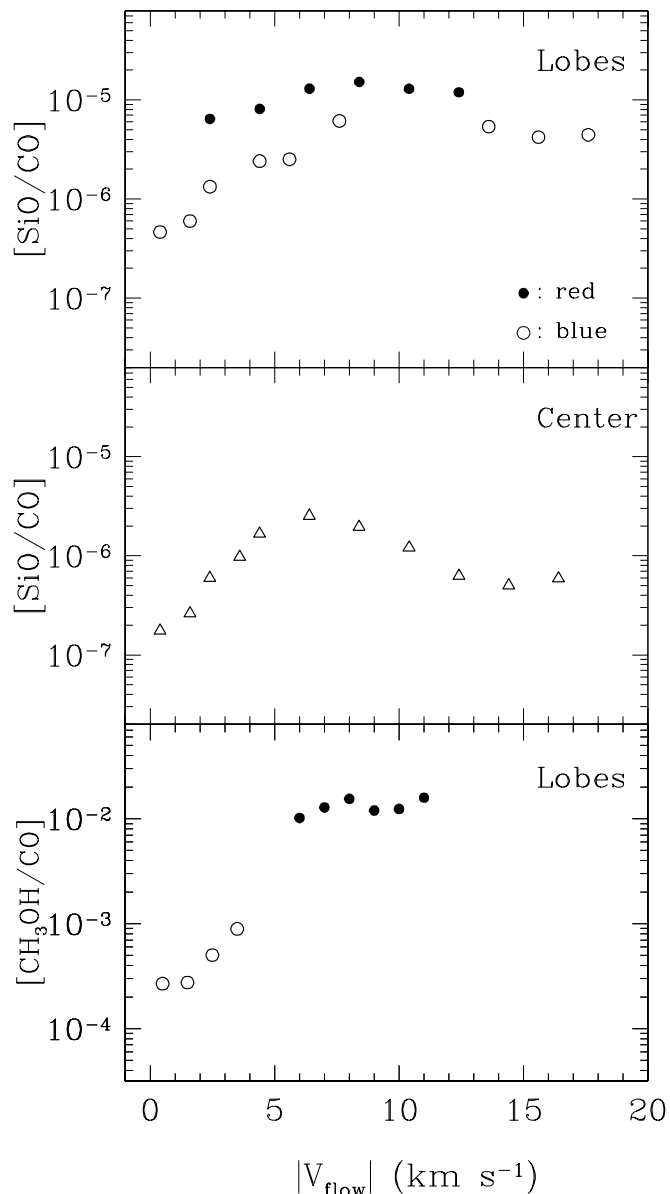

FIG. 6.—Abundances relative to CO vs. absolute value of flow velocity. *Top:* [SiO/CO] vs. $|v_{flow}|$ at the peak position of the outflow lobes. *Middle:* [SiO/CO] vs. $|v_{flow}|$ at the central position. *Bottom:* [CH$_3$OH/CO] vs. $|v_{flow}|$ at the peak position of the outflow lobes. Open and filled circles correspond to values derived at the peak position of the blueshifted lobe and redshifted lobe, respectively.

Figure 6. The [SiO/CO] abundance ratios are typically $\sim 10^{-5}$ toward the lobes and $\sim 10^{-6}$ toward the central position.

To quantitatively assess the chemical changes of the ambient medium due to the outflow phenomena requires a knowledge of the chemical abundances of the quiescent ambient gas. The abundances of methanol and silicon monoxide in the ambient gas of NGC 2071 are not known, however. In dark clouds the [CH$_3$OH/CO] abundance ratio is 3×10^{-5} (Friberg et al. 1988; van Dishoeck et al. 1993), whereas for the [SiO/CO] abundance ratio only an upper limit of less than 3×10^{-8} exists (Ziurys, Friberg, & Irvine 1989; van Dishoeck et al. 1993). In the following we assume that the abundance ratios in the ambient gas of NGC 2071 are similar to those in dark clouds. The enhancements, relative to quiescent ambient gas in dark globules, of the gas phase silicon monoxide and methanol in the outflow lobes of NGC 2071 are given in the sixth column of Tables 2 and 3, respectively. The enhancement of the [SiO/CO] abundance ratios are larger in the southwest clump (peak enhancement ≥ 500) than in the northeast clump (peak enhancement ≥ 170) by a factor of ~ 3. The peak enhancement in the [CH$_3$OH/CO] abundance ratio is ~ 500 in the southwest clump and ~ 70 in the northwest clump. The high abundance of SiO molecules in the lobes of molecular outflows, is most likely due to the injection into the gas phase by shocks of Si atoms and/or Si-bearing species. Once silicon is injected into the gas phase, chemical models based on ion-molecule reactions predict a large abundance of SiO molecules (Turner & Dalgarno 1977; Hartquist et al. 1980). The enhancement of CH$_3$OH molecules is, on the other hand, thought to be produced by the evaporation of ice mantles (Charnley, Tielens, & Millar 1992) due to heating by low-velocity shocks, since volatile species, such as CH$_3$OH, HCN, and H$_2$CO, can only survive sputtering or desorption of grain mantles at low shock velocities ($v_s \leq 10$ km s^{-1}).

Figure 6 shows a trend indicating an increase of SiO enhancement with $|v_{\mathrm{flow}}|$ at low flow velocity, whereas for $|v_{\mathrm{flow}}| > 5$ km s^{-1} the enhancement is roughly independent of flow velocity. On the other hand, the [CH$_3$OH/CO] abundance ratios exhibit a clear increase with flow velocity, from $\sim 3 \times 10^{-4}$ at low flow velocities to $\sim 1 \times 10^{-2}$ at intermediate flow velocities. Since the values at low and intermediate flow velocities were determined from observations of the blueshifted lobe and redshifted lobe, respectively, this trend cannot be interpreted as reflecting an actual velocity selective enhancement caused by shocks. It is probably produced by the differences in the physical conditions of the preshock gas toward the northeast and southwest clumps. In the following we discuss the enhancement toward each lobe individually.

4.3.1. Southwest Clump

The moderate velocity of the ambient shock in the red-shifted lobe ($v_s \sim 12$ km s^{-1}), not fast enough to dissociate molecules, suggests that the production of molecular species in the southwest clump is due to the presence of C-type shocks. In particular the synthesis of molecules from atoms and ions can be highly efficient behind nondissociative C-type shocks. The main mechanism of injection of silicon is sputtering of Si-bearing material in grains driven by neutral particle impact on charged grains (Draine 1995; Flower & Pineau des Forêts 1995; Schilke et al. 1997);

although grain-grain collisions can be important for low-velocity shocks ($25 \lesssim v_s \lesssim 35$ km s^{-1}) in dense regions ($n(\mathrm{H}_2) > 5 \times 10^5$ cm^{-3}; Caselli et al. 1997). The sputtering of Si-bearing material can arise from either grain cores, namely, refractory grains that are composed of silicates and graphites, or from grain mantles (Schilke et al. 1997). The release of Si-bearing material from grain cores requires higher impact energies than the release from mantles; substantial erosion of ice mantles can occur in C-shocks with velocities of ~ 25 km s^{-1}, while shock speeds of ~ 55 km s^{-1} are required in order to significantly erode the grain cores by He impacts. The inclusion of heavier species, such as CO and H$_2$O, can significantly lower the impact energies required for the erosion of grain cores, so that shock velocities as low as 25 km s^{-1} can cause substantial erosion of the grain cores (Schilke et al. 1997).

We find that at the peak position of the southwest clump the total column density of SiO is 7×10^{12} cm^{-2} and that the column density of CH$_3$OH, in the range of flow velocity from 5.5 to 11.5 km s^{-1}, is 3×10^{15} cm^{-2}. Though the C-type shock models are still preliminary, most are able to explain column densities of SiO in molecular outflows of the observed order. From the observed velocity integrated SiO(2 → 1) emission, of 3.2 K km s^{-1}, using the results from the C-type shock model of Schilke et al. (1997) for a density of 10^5 cm^{-3} (see their Fig. 8), we obtain $v_s \sim 13$ km s^{-1}, in good agreement with the value estimated in § 4.1. For this moderate shock velocity, the silicon injected in the gas phase is mainly released from the mantle of the grains by heavy particle sputtering, the contribution from dust core sputtering being negligible. None of the published C-type shock models have, however, considered the production of methanol. We suggest that the large abundance of methanol, one of the most abundant ices on grain surfaces, in the southwest clump arises from the evaporation of ice mantles (Tielens & Allamandola 1987; Bachiller et al. 1998; Blake et al. 1991) produced by the low-velocity shock.

4.3.2. Northeast Clump

We find that the total column density of SiO toward the peak of the northeast clump is 1×10^{13} cm^{-2}, which is similar to that of the southwest clump. On the other hand, the column density of CH$_3$OH in the flow velocity range from -11.5 to -5.5 km s^{-1} is at least 2 orders of magnitude lower than that derived toward the southwest clump in the corresponding flow velocity range ($5.5 < v_{\mathrm{flow}} < 11.5$ km s^{-1}). These results most likely reflect the larger flow velocities, $v_s \sim 45$ km s^{-1}, attained toward the northeast clump. Models of the chemistry in regions behind fast dissociative shocks predict a substantial enhancement in the abundance of SiO molecules (Neufeld & Dalgarno 1989). In particular, for a shock with a velocity of 60 km s^{-1} propagating in a gas with preshock density of 10^4 cm^{-3} (the closest values to those of the northeast clump) the predicted column density of SiO molecules is 4×10^{12} cm^{-2}, close to that derived from the observations. On the other hand, at this high shock velocities volatile species, such as CH$_3$OH, do not survive sputtering or desorption of grain mantles. We suggest that in the northeast clump a considerable fraction of the SiO molecules are formed behind a dissociative shock, with little methanol being produced behind the shock. The low-velocity SiO gas may arise as the high-velocity SiO shocked gas is subsequently slowed down by sweeping up ambient material.

5. SUMMARY

The highly collimated NGC 2071 bipolar outflow has been observed, using the SEST telescope, in lines of silicon monoxide and methanol. The main results and conclusions presented in this paper are summarized as follows.

SiO emission is detected toward the lobes as well as toward the central core region and over a wide range in velocity, from v_{LSR} of -23 to 28 km s^{-1}. The spatial distribution of the SiO wing emission shows three distinct features: a blueshifted clump located toward the northeast, a redshifted clump located toward the southwest, and a central structure, with moderate redshifted velocities, located near the cluster of young stellar objects. The shape of the SiO profiles from the blueshifted and redshifted clumps are distinctly different. The SiO lines from the northeast clump exhibit a peak near the velocity of the ambient cloud and a gradual decline toward blueshifted velocities reaching radial flow velocities of up to -32 km s^{-1}. On the other hand, the SiO profiles from the southwest clump show a peak emission at a velocity that is redshifted by ~ 8.5 km s^{-1} from the ambient gas velocity and a gradual decline in brightness toward the ambient cloud velocity.

The redshifted SiO clump has a deconvolved size (FWHM) of $\sim 47''$, its peak position is offset from the central sources by $\sim 130''$ toward the southwest, and lies nearly at the outer edge of the swept-up redshifted CO lobe. We propose that the SiO emission from the southwest clump arises from swept-up ambient molecular gas that has been accelerated abruptly by the working surface driven by a high-velocity collimated jet. The entrainment of ambient gas into the jet flow takes place mainly at the working surface of the jet (prompt entrainment) producing the observed molecular SiO outflow with a radial outflow velocity of ~ 8.5 km s^{-1}. Adopting a jet velocity of 200 km s^{-1} we imply the presence of a light jet, with $\rho_j/\rho_a = 4 \times 10^{-3}$. Further, assuming an ambient density of 1×10^5 cm^{-3} we derive that the jet density is $\rho_j \sim 4 \times 10^2$ cm^{-3}.

The blueshifted SiO clump has a deconvolved size (FWHM) of $\sim 47''$, a peak position located $\sim 77''$ northeast from the central energy sources, and lies roughly halfway along the blueshifted swept-up CO lobe. It is spatially coincident with a broad blueshifted velocity feature detected in SO by Chernin & Masson (1993), both of which exhibit terminal radial flow velocities of ~ -32 km s^{-1}. We suggest that toward the northeast the collimated jet is interacting with a less dense medium than that toward the southwest, resulting in a high-velocity bow shock, which may be dissociative at its apex. SiO emission arises from material in the wake of the working surface, where the shocked material is decelerating rapidly.

We find that the abundance of silicon monoxide is enhanced, with respect to that of quiescent ambient gas in dark globules, by a factor of at least 500 in the southwest clump and 170 in the northeast clump. The abundance of methanol is considerably more enhanced toward the southwest clump (peak enhancement of ~ 500) than toward the northwest clump (peak enhancement of ~ 70). We suggest that the large enhancements of methanol and silicon monoxide in the outflow clumps are most likely due to the release from grains of ice mantles and Si-bearing species via shocks produced by the interaction between the outflow and dense ambient gas. The derived column densities of SiO (and hence enhancements) can be well explained by C-type shock models with moderate velocities ($v_s \sim 13$ km s^{-1}) for the southwest clump and by a faster bow shock ($v_s \sim 45$ km s^{-1}) for the northeast clump. The high abundance of methanol in the southwest clump is attributed to efficient sputtering or desorption from grain mantles of volatile species by the associated low velocity shock. The evaporated molecules subsequently drive a rapid gas phase chemistry leading to complex organic molecules. On the other hand, at the high shock velocity attained at the northeast clump volatile species, such as CH_3OH, do not survive and hence the low abundance of methanol toward this clump.

REFERENCES

Anthony-Twarog, B. J. 1982, AJ, 87, 1213
Avery, L. W., & Chiao, M. 1996, ApJ, 463, 642
Bachiller, R. 1996, ARA&A, 34, 111
Bachiller, R., Codella, C., Colomer, F., Liechti, S., & Walmsley, C. M. 1998, A&A, 335, 266
Bachiller, R., & Gómez-Gonzalez, J. 1992, A&A Rev., 3, 257
Bachiller, R., Liechti, S., Walmsley, C. M., & Colomer, F. 1995, A&A, 295, L51
Bachiller, R., Martín-Pintado, J., & Fuente, A. 1991, A&A, 243, L21
Bachiller, R., & Pérez Gutiérrez, M. 1997, ApJ, 487, L93
Bally, J. 1982, ApJ, 261, 558
Bally, J., & Lada, C.J. 1983, ApJ, 265, 824
Bally, J., & Lane, A.P. 1982, ApJ, 257, 612
Bally, J., & Predmore, R. 1983, ApJ, 265, 778
Blake, D., Allamandola, L., Sandford, S., Hudgings, D., & Freund, F. 1991, Science, 254, 548
Blake, G. A., Sandell, G., van Dishoeck, E. F., Groesbeck, T. D., Mundy, L. G., & Aspin, C. 1995, ApJ, 441, 689
Blake, G. A., Sutton, E. C., Masson, C. R., & Phillips, T. G. 1987, ApJ, 315, 621
Bourke, T. L., et al. 1997, ApJ, 476, 781
Burton, M. G., Geballe, T. R., & Brand, P. W. J. L. 1989, MNRAS, 238, 1513
Butner, H. M., Evans, II, N. J., Harvey, P. M., Mundy, L. G., Natta, A., & Randich, M. S. 1990, ApJ, 364, 164
Campbell, P. D. 1978, PASP, 90, 262
Caselli, P., Hartquist, T. W., & Havnes, O. 1997, A&A, 322, 296

Charnley, S. B., Tielens, A. G. G. M., & Millar, T. J. 1992, ApJ, 399, L71
Chernin, L. M., & Masson, C. R. 1992, ApJ, 396, L35
———. 1993, ApJ, 403, L21
Chernin, L. M., Masson, C.R., Gouveia Dal Pino, E. M., & Benz, W. 1994, ApJ, 426, 204
Choi, M., Evans II, N. J., & Jaffe, D. T. 1993, ApJ, 417, 624
Draine, B. J. 1995, A&AS, 233, 111
Draine, B. J., Roberge, W. G., & Dalgarno, A. 1983, ApJ, 264, 485
Flower, D. R., & Pineau des Forêts, G. 1995, MNRAS, 275, 1049
Friberg, P., Madden, S. C., Hjalmarson, Å., & Irvine, W.M. 1988, A&A, 195, 281
Fukui, Y., Iwata, T., Mizuno, A., Bally, J., & Lane, A.P. 1993, in Protostars and Planets III, ed. E. H. Levy & J. I. Lunine (Tucson: The Univ. Arizona Press), 603
Garay, G., Köhnenkamp, I., Bourke, T. L., Rodríguez, L. F., & Lehtinen, K. K. 1998, ApJ, 509, 768
Garden, R. P., Russell, A. P. G., & Burton, M. G. 1990, ApJ, 354, 232
Genzel, R., & Downes, D. 1979, A&A, 72, 234
Girart, J. M., Ho, P. T. P., Rudolph, A. L., Estalella, R., Wilner, D. J., & Chernin, L. M. 1999, ApJ, 522, 921
Hartquist, T. W., Oppenheimer, M., & Dalgarno, A. 1980, ApJ, 236, 182
Harvey, P. M., Campbell, M. F., Hoffmann, W. F., Thronson, H. A., & Gatley, I. 1979, ApJ, 229, 990
Hollenbach, D. 1997, in IAU Symp. 182, Herbig-Haro Flows and the Birth of Low Mass Stars, ed. B. Reipurth & C. Bertout (Dordrecht: Reidel), 181
Hollenbach, D., & McKee, C. F. 1989, ApJ, 342, 306

Kitamura, Y., Kawabe, R., & Ishiguro, M. 1992, PASJ, 44, 407
Kitamura, Y., Kawabe, R., Yamashita, T., & Hayashi, M. 1990, ApJ, 363, 180
Kwan, J. 1977, ApJ, 216, 713
Lane, A. P., & Bally, J. 1986, ApJ, 310, 820
Lichten, S. M. 1982, ApJ, 253, 593
Linke, R. A., Frerking, M. A., & Thaddeus, P. 1978, ApJ, 234, L139
Margulis, M., & Snell, R. L. 1989, ApJ, 343, 779
Martín-Pintado, J., Bachiller, R., & Fuente, A. 1992, A&A, 254, 315
Masson, C. R., & Chernin, L. M. 1993, ApJ, 414, 230
Mitchell, G. F. 1984, ApJ, 287, 665
Moriarty-Schieven, G. H., Snell, R. L., & Hughes, V. A. 1989, ApJ, 347, 358
Mundt, R. 1986, Canadian J. Phys., 64, 407
Mundt, R., Brugel, E. W., & Bührke, T. 1987, ApJ, 319, 275
Neufeld, D. A., & Dalgarno, A. 1989, ApJ, 340, 869
Pankonin, V., Winnberg, A., & Booth, R. S. 1977, A&A, 58, L25
Persson, S. E., Geballe, T. R., Simon, T., Lonsdale, C., & Baas, F. 1981, ApJ, 251, L81
Raga, A. C., & Cabrit, S. 1993, A&A, 278, 267
Reipurth, B. 1991, The Physics of Star Formation and Early Stellar Evolution, ed. C. J. Lada & N. D. Kylafis (Dordrecht: Kluwer), 497
Richer, J. S., Hills, R. E., & Padman, R. 1992, MNRAS, 254, 535
Ruiz, A., Rodríguez, L. F., Cantó, J., & Mirabel, I. F. 1992, ApJ, 398, 139
Sargent, A. I., van Duinen, R. J., Fridlund, C. V. M., Nordh, H. L., & Aalders, J. W. G. 1981, ApJ, 249, 607

Schilke, P., Walmsley, C. M., Pineau des Forêts, G., & Flower, D. R. 1997, A&A, 321, 293
Schwartz, P. R., & Buhl, D. 1975, ApJ, 201, L27
Scoville, N. Z., Sargent, A. I., Sanders, D. B., Claussen, M. J., Masson, C. R., Lo, K. Y., & Phillips, T. G. 1986, ApJ, 303, 416
Simon, T., & Joyce, R. R. 1983, ApJ, 265, 864
Smith, M. D., & Brand, P. W. J. L. 1990, MNRAS, 245, 108
Snell, R. L., & Bally, J. 1986, ApJ, 303, 683
Snell, R. L., Scoville, N. Z., Sanders, D. B., & Erickson, N. R. 1984, ApJ, 284, 176
Tielens, A. G. G. M., & Allamandola, L. J. 1987, in Physical Processes in Interstellar Clouds, ed. G. E. Morfill & M. Scholer (Dordrecht: Reidel), 333
Torrelles, J. M., Gómez, J. F, Rodríguez, L. F., Curiel, S., Anglada, G., & Ho, P. T. P. 1998, ApJ, 505, 756
Turner, J. L., & Dalgarno, A. 1977, ApJ, 213, 386
van Dishoeck, E. F., Blake, G. A., Draine, B. T., & Lunine, J. I. 1993, in Protostars and Planets III, ed. E. H. Levy & J. Lunine (Tucson: Univ. Arizona Press), 163
Walther, D. M., Geballe, T. R., & Robson, E. I. 1991, ApJ, 377, 246
Walther, D. M., Robson, E. I., Aspin, C., & Dent, W. R. F. 1993, ApJ, 418, 310
Wootten, A., Loren, R. B., Sandqvist, A., Friberg, P., & Hjalmarson, A. 1984, ApJ, 279, 633
Ziurys, L. M., Friberg, P., & Irvine, W. M. 1989, ApJ, 343, 201